ACS NANO

www.acsnano.org

ARTICLE

# Vapor Infiltration Synthesis of Indium Sulfide Magic Size Cluster

Kihoon Kim, Shana Havenridge, Nestor J. Zaluzec, Donghyeon Kang, Nuwanthaka P. Jayaweera, Jeffrey W. Elam, Karen L. Mulfort, Cong Liu, and Alex B. F. Martinson*

Cite This: *ACS Nano* 2024, 18, 31372–31380

Read Online

ACCESS | Metrics & More | Article Recommendations | Supporting Information

**ABSTRACT:** **The energetically favorable formation of atomically precise clusters, known as magic size clusters, in the solution phase enables a precision nanoscale synthesis with exquisite uniformity. We report the synthesis of magic size clusters via vapor infiltration of atomic layer deposition precursors directly in a polymer thin film. Sequential infiltration of trimethylindium vapor and hydrogen sulfide gas into poly(methyl methacrylate) leads to the formation of clusters with uniform properties consistent with a magic size cluster—$In_6S_6(CH_3)_6$. While an increase in cluster size might be expected with additional sequential infiltration cycles of the reactive In and S precursors, uniform properties consistent with magic size clusters form in multiple polymers under a range of processing conditions. Ultraviolet−visible absorption spectra of $In_6S_6(CH_3)_6$ are largely independent of the number of sequential infiltration cycles and exhibit air stability, both of which are attributed to an energetically favorable synthetic pathway that is evaluated with density functional theory.**

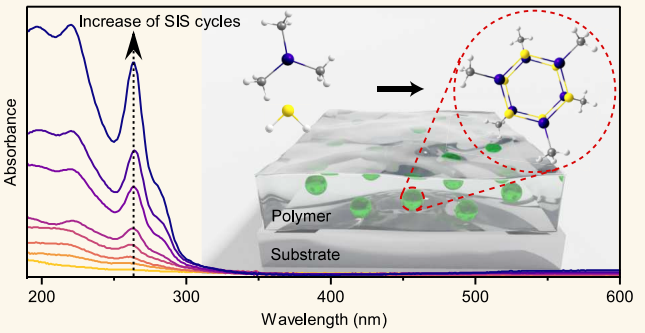


**KEYWORDS:** *sequential infiltration synthesis, atomic layer deposition, cluster, semiconductor, metal chalcogenide*



Colloidal semiconductors are a versatile class of materials with optoelectronic properties tuned through crystal structure, size, shape, composition, and surface termination to suit numerous applications. Despite the improvements in synthetic precision of colloidal material, however, the synthesis typically produces a distribution of atomic structures that result in measurable inhomogeneity in the resulting properties.[1,2] Magic size clusters (MSCs) are a subclass of colloidal nanocrystals with molecularly precise arrangements of countable atom numbers that exhibit extreme homogeneity.[3−5] Energetically favorable intermediate species that assemble into larger nanomaterial assemblies often reveal mechanistic details into nucleation and growth.[5−11] The unique atomic arrangements can also result in exceptional properties not achievable through bulk structures.[1,6,7,12,13] Nearly all studies of MSCs utilize solution phase synthetic methods, which inherently struggle to achieve nucleation control, separation of metastable species, solubility of the product, and concentration/fabrication into thin film format.[1,14,15]

Sequential infiltration synthesis (SIS) is a chemical vapor deposition method that is derived from atomic layer deposition (ALD), in which chemical precursors are sequentially exposed to a solid substrate surface to grow a conformal thin film coating. In contrast to ALD, SIS is intended to deposit materials *within* a soft substrate (e.g., a polymer film), with multiple cycles resulting in more deposition through swelling of the soft matrix material.[16−19] Inert gas purging after the alternate introduction of each vapor precursor enables the facile purification of the resulting deposit through the volatilization of unreacted precursors and reaction byproducts. Over the past decade, the expanding SIS process library for metal oxides has been leveraged for a range of applications including enhanced mechanical and optical performance, nanopatterning, photovoltaics, and membranes.[20−33] More recently, a small subset of SIS processes has been suggested to result in a distribution of molecular level clusters.[17−19] For example, controlled nucleation and precision growth can be achieved through strategic selection of the SIS dosing schedule to produce inorganic cluster sizes that roughly scale with the number of growth cycles.[34]

Received: August 9, 2024
Revised: October 17, 2024
Accepted: October 23, 2024
Published: November 1, 2024





https://doi.org/10.1021/acsnano.4c10943
*ACS Nano* 2024, 18, 31372−31380

Metal chalcogenide materials possess rich photophysical properties with potential applications in several fields. Due largely to highly polarizable chalcogen centers, their properties are distinct from the corresponding metal oxides.[35−37] For example, while $In_2O_3$ is transparent to visible light, $In_2S_3$ exhibits several polymorphic structures that have been regarded as promising materials for photodetectors, solar energy absorption, and photocatalysis including water splitting, and reduction of $CO_2$.[38−42] Many chalcogenide materials have been deposited in thin film form via ALD.[43,44] However, the SIS of metal chalcogenides remains unexplored, and the molecular-level synthesis of a metal chalcogenide cluster via SIS has not been previously reported.

Here we report the synthesis of a metal chalcogenide in polymer thin films via SIS and hypothesize the formation of a molecular cluster, namely $In_6S_6(CH_3)_6$. In contrast to traditional ALD and SIS growth mechanisms, we find no evidence for increasing deposit size after 5 SIS cycles, but instead observe only an increasing concentration of the MSC in the polymer matrix. The same SIS process performed at a lower deposition temperature alters the reaction pathway away from the MSC and toward a less homogeneous population of clusters with limited atmospheric stability. Compared to the solution phase synthesis of MSCs, this SIS approach affords ready control over the nucleation density and controlled diffusion of metastable species to produce concentrated MSCs that are conveniently fabricated in thin film format.

## RESULTS AND DISCUSSION

Initial efforts to deposit $InS_x$ clusters via SIS were informed by our previous discovery of SIS-derived $InO_x$-based deposits in PMMA.[19,34] Trimethylindium (TMIn) was previously shown to infiltrate PMMA and form a reversible Lewis acid−base adduct with the carbonyl oxygen in the methacrylate backbone. Adduct formation increases the residence time of TMIn in the polymer matrix, enabling an adjustable concentration of TMIn in the swollen polymer after briefly pumping out vapor phase TMIn from the reactor (Scheme 1). The infiltration of $H_2S$ gas is hypothesized to result in the proton-mediated exchange of at least one methyl to bind sulfhydryl and release methane, thereby nucleating a monometallic $InS_x$ species according to the general reaction scheme:

$$In(CH_3)_3 + H_2S \rightarrow In(CH_3)_{3-x}(SH)_x + xCH_4 \quad (1)$$

where x = 1, 2, or 3. Subsequent reaction of the $InS_x$ monomers may result in larger clusters. The incorporation of an $InS_x$ deposit into a PMMA film was most simply confirmed through UV−visible absorbance spectroscopy of substrates subjected to SIS processing with and without PMMA, TMIn, and $H_2S$ exposure (Figure 1). When either TMIn or $H_2S$ precursors were omitted, no distinct change in absorbance was observed. This suggests that there is little to no irreversible reaction of TMIn or $H_2S$ with PMMA as expected upon sufficient $N_2$ purging under low vacuum. In contrast, alternating doses of TMIn and $H_2S$ (i.e., complete SIS cycles) produce strong and clear absorbance features at 200, 220, and 264 nm as well as a shoulder at 280 nm.

**Scheme 1. Synthetic Process of 1 SIS Cycle To Form $InS_x$**[a]

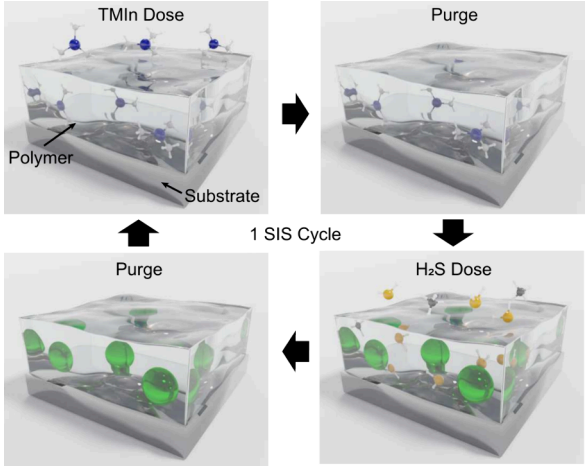


[a]Green spheres represent $InS_x$ cluster as a result of reaction between TMIn and $H_2S$.

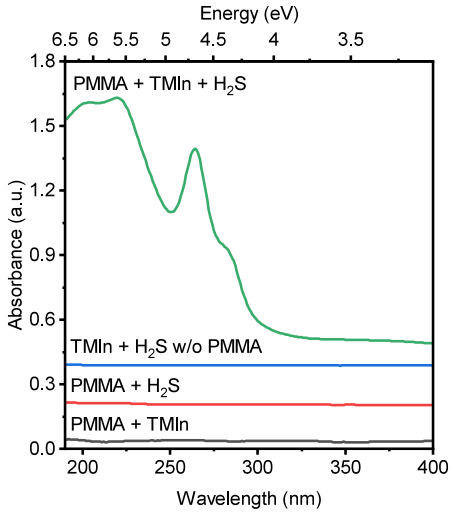


**Figure 1. UV−visible absorbance change after complete or partial SIS processing at 160 °C. 70 SIS cycles were applied for each condition and spectra are offset for clarity. The thickness of PMMA is fixed to 300 nm and the absorbance of the polymer thin films and fused silica substrate are subtracted from each spectrum. The absence of either TMIn, $H_2S$, or PMMA results in little to no deposition.**

A relatively high SIS processing temperature (160 °C) and long $N_2$ purging (480 s) promote efficient dissociation and removal of TMIn adduct, however, any remaining TMIn reacts with the subsequently dosed $H_2S$ to form $InS_x$.[18−20] No remarkable absorbance spectrum was observed with alternate dosing in the absence of a PMMA film, suggesting that the TMIn-PMMA adduct favors $InS_x$ deposition. When the peak at 264 nm was fitted with a single Gaussian curve, its full width at half-maximum height was 21 nm (0.38 eV) (see Supporting Information Figure S1), which is consistent with a sharp absorbance feature from a homogeneous molecular cluster prepared in a solution phase.[10] The UV−visible absorbance spectra of the SIS-derived $InS_x$ species are also distinct from previously reported nanoscale $InS_x$ including 2D $\beta$-$In_2S_3$ flakes (low energy absorbance peak at <700 nm), $In_{38}S_{65}$ super-tetrahedral cluster (featureless band edge at 3 eV), and $In_4S_4$ clusters with four ligands of 1,10-phenanthroline (low energy absorbance peak at <440 nm).[39,45,46]



https://doi.org/10.1021/acsnano.4c10943
ACS Nano 2024, 18, 31372−31380

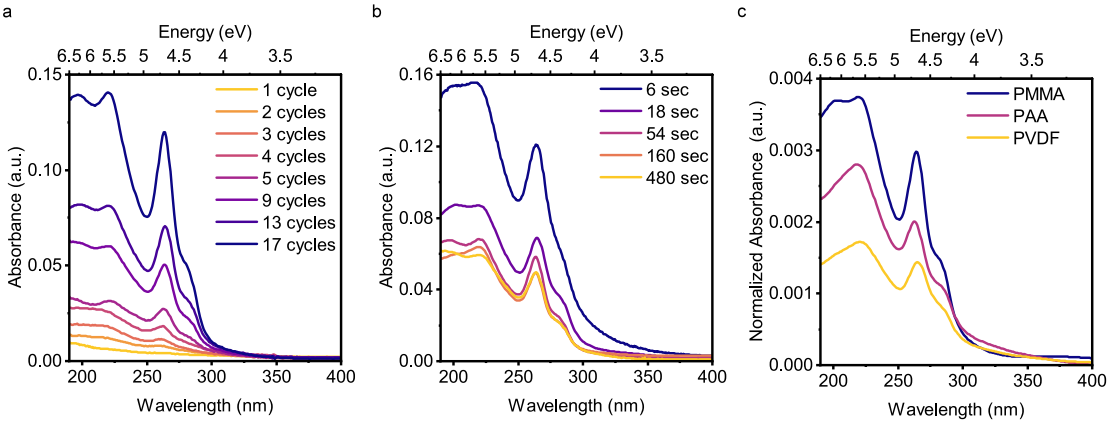


**Figure 2. MSC formation. UV−visible absorbance spectra (a) as a function of SIS cycle number while $N_2$ purging time was fixed to 480 s, (b) after 9 SIS cycles with varying $N_2$ purging time, and (c) after identical 70 SIS cycles in PMMA, PAA, and PVDF. The absorbance was divided by the initial thickness of polymer in order to correct for film thickness variations.**

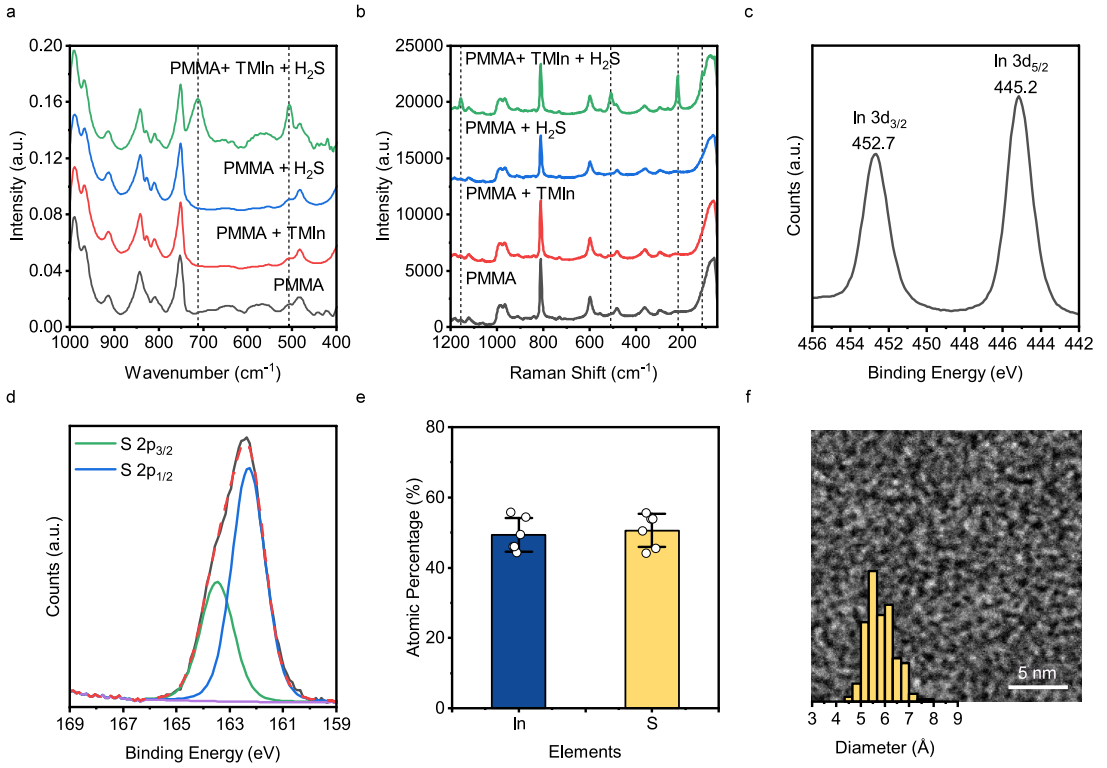


**Figure 3. Structure analysis of $InS_x$ cluster. (a) FTIR and (b) Raman spectra after complete or partial SIS processing at 160 °C. Each dosing condition was repeated 70 times. The vertical dashed lines indicate the peak positions which were observed only after alternating doses of TMIn and $H_2S$. (c) In 3d spectrum, (d) S 2p spectrum, and (e) Stoichiometry of In and S from XPS after 70 SIS cycles. Seven different samples were measured for statistical analysis and error bars represent standard deviation. (f) STEM image of $InS_x$ cluster after 5 SIS cycles. A statistical analysis of cluster diameter (inset) uses 0.33 Å binning of 200 clusters. The scale was calibrated with the d ⟨111⟩ interatomic spacing of 2.355 Å of Au.**

Cluster formation was investigated through an evaluation of the UV−visible absorbance spectrum under variable reaction conditions. First, the SIS cycle number dependence on absorbance was probed to understand nucleation and growth, Figure 2a. Despite moderate signal-to-noise at the lowest SIS cycle numbers, absorbance at wavelengths <300 nm is observed after even a single TMIn + $H_2S$ cycle. With a greater SIS cycle number, the overall absorbance increases and features at 264, 220, and 200 nm are more clearly developed. The cycle-dependent absorbance peak intensity at 264 nm increased approximately linearly up to 13 SIS cycles and then followed a shallow quadratic (slightly superlinear) function upon greater cycle numbers (Supporting Information Figure S2). Normalized UV−visible spectra reveal that after 5 cycles the line shape of absorbance is constant and does not significantly alter up to at least 70 cycles. This implies that the majority cluster structure is constant after 5 SIS cycles, and only the concentration of the cluster increases upon additional SIS cycles, consistent with the hypothesis for MSCs formation. Fixing the SIS cycle number to 9, the $N_2$ purging time was



https://doi.org/10.1021/acsnano.4c10943
ACS Nano 2024, 18, 31372−31380

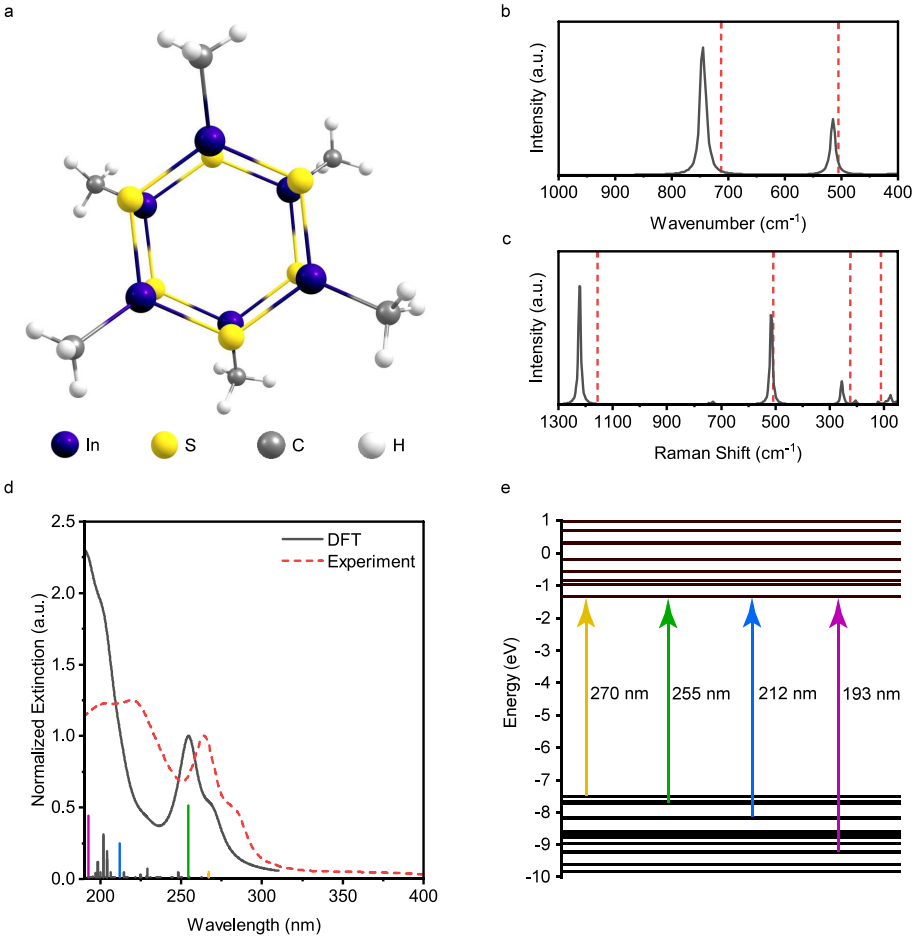


**Figure 4. First-principles computation and simulation of $In_6S_6(CH_3)_6$ at the MN15/CEP-121G level of theory. (a) DFT optimized structure of $In_6S_6(CH_3)_6$, and simulated (b) IR, and (c) Raman spectra of $In_6S_6(CH_3)_6$. The vertical dashed red lines correspond to peak positions from experimental data (see Figure 3). (d) The UV−vis absorbance spectrum simulated from DFT (black solid) overlaid with the experimental absorbance spectra of the MSC (red dashed). (e) Representative molecular orbital transitions responsible for the absorbance peaks in the calculated spectrum. Each color of transition corresponds to the color of the stick spectrum in (d).**

varied from 6 to 480 s to investigate the effect of TMIn concentration (Figure 2b). As the purging time is decreased below 160 s, the absorbance intensity increases exponentially, consistent with the reaction of a larger concentration of the TMIn adduct remaining in the PMMA film. Despite the change in the absorbance intensity, the spectral line shape remained nearly the same, further supporting the hypothesis for MSCs formation (see normalized data in Supplementary Figure 2). Slight variation in the measured line shape may result from imperfect absorbance subtraction due to changes in the thick film interference from the PMMA matrix, which variably swells with the addition of variable cluster density. The robustness of MSC formation is further revealed by the application of the same SIS process to an alternative polymer, since polymer thin films serve an analogous role to the solvent in solution phase synthesis. In the solution phase synthesis of colloidal nanocrystals, the choice of solvent often affects the resulting nanocrystals' size, shape, and crystallinity.[47−51] As such, a change of the functional group in the polymer could influence the resulting cluster structure. Polyacrylic acid (PAA) and Polyvinylidene fluoride (PVDF) were both considered as both carboxylic acid and fluorine are known to interact with In cations.[52,53] Despite the different polymer functional groups, we observe identical MSC optical absorption spectra, which suggests that identical MSCs are formed (Figure 2c). Only the intensity of UV absorbance decreased from PMMA to PAA to PVDF, which implies that the concentration of the cluster depends on the properties of the polymer, including functional group interaction.

Initial structure analysis of the MSCs was performed by vibrational spectroscopy. The infrared absorbance spectra reveal that in the absence of either TMIn or $H_2S$, only the vibration features of PMMA are reproduced, Figure 3a. Vibrational spectroscopy further confirmed that only alternating doses of TMIn and $H_2S$ in PMMA produce a clear change that can be attributed to the $InS_x$ cluster, here at 715 and 505 $cm^{-1}$. These two peak positions are similar but not identical to TMIn features for methyl rocking and In−C asymmetric stretch.[54,55] Although the $InS_x$ cluster was concentrated through 70 SIS cycles, no remarkable change of the PMMA carbonyl group at 1731 $cm^{-1}$ was observed, which implies minimal interaction with PMMA (see Supporting Information Figure S3).[19] Additional vibrational structural information was obtained from Raman spectroscopy, where again no remarkable changes in Raman intensity were detected after dosing only TMIn or $H_2S$ (see Figure 3b). However, clear Raman peaks are observed at 114, 220, 507, and 1154 $cm^{-1}$ upon cluster formation. These Raman features are also more similar


https://doi.org/10.1021/acsnano.4c10943
ACS Nano 2024, 18, 31372−31380

to those previously measured for TMIn than for bulk $In_2S_3$, particularly the methyl-related peaks at 507 and 1154 $cm^{-1}$.[39,55] As such, we hypothesize that some methyl groups are preserved in the final cluster structure. In the case of a proton-mediated ligand exchange reaction of $H_2S$ with TMIn without further reaction, one might expect that thiol groups may be detected upon exchange of methyl groups. However, thiol-related features (around 2450 $cm^{-1}$) were not observed in either IR or Raman spectra (see Supporting Information Figure S3).[44,56] The lack of a thiol feature is consistent with incomplete methyl exchange and prompt subsequent reaction of thiol-terminated molecular fragments or a combination thereof. The incomplete reaction of ligands at metal centers is a well-known phenomenon in solution phase synthesis.[47,53] Previous ALD and density functional theory (DFT) studies also suggest that incomplete ligand removal is possible, leading to ligand incorporation in the deposited materials.[57−59] Elemental analysis of In and S by X-ray photoelectron spectroscopy (XPS) reveals two In 3d peaks at 445.2 and 452.7 eV (Figure 3c).[60,61] The S 2p peak was fitted with two peaks ($2p_{1/2}$ and $2p_{3/2}$) without the need for other derivative formation (e.g., S−O bonding) (Figure 3d). Despite the similar binding energy of both In and S to bulk $In_2S_3$, the XPS signal intensities indicate a nearly stoichiometric ratio (1:1) between In and S, Figure 3d, that significantly deviates from stoichiometric bulk compounds and from clusters previously synthesized in the solution phase (e.g., 38:65 for $In_{38}S_{65}$).[46,61] Finally, attempts to directly image the small clusters with high resolution Scanning Transmission Electron Microscopy (STEM) were not clearly resolved but suggest deposits with a small size (~6 Å, Figure 3d). While the accuracy of the subnanometer scale measurement is low, the subnanometer, uniform cluster size is consistent with the formation of molecular MSCs. Hyperspectral elemental intensity distribution imaging supports a cluster comprising In and S atoms but is unable to probe methyl termination, given the relatively low atomic weight of C and H (Supporting Information Figure S4).

DFT was leveraged to evaluate structures and simulate spectra for comparison to experiments. First, the IR, Raman, and UV−visible absorbance spectra of cluster structures with variable numbers of In and S atoms and methyl group terminations were calculated. The search emphasized structures with a 1:1 stoichiometry between In and S, which narrows the number of possible nanocluster configurations. From the theoretically optimized structures, details of $In_2S_2(CH_3)_2$, $In_3S_3(CH_3)_3$, $In_4S_4(CH_3)_4$, and $In_9S_9(CH_3)_9$ were further investigated (Supporting Information Figure S5) before an $In_6S_6(CH_3)_6$ cluster with stacked and rotated hexagon, in the $D_3$ point group (Figure 4a), was selected as the most likely MSC. All of the structures considered include methyl terminated In, resulting in common simulated IR peaks near 741 and 516 $cm^{-1}$ due to methyl rocking and In−C stretch, respectively (e.g., Figure 4b). Simulated Raman peaks corresponding to In−C symmetric stretching and methyl group scissoring near 507 $cm^{-1}$ and 1154 $cm^{-1}$ were also observed for most configurations (e.g., Figure 4c). However, $In_2S_2(CH_3)_2$ and $In_4S_4(CH_3)_4$ show a large discrepancy of the 220 $cm^{-1}$ In−S core feature relative to hexagonal $In_3S_3(CH_3)_3$ based ones. Among these structures, the simulated UV−visible absorbance spectrum of $In_6S_6(CH_3)_6$ shows a spectral line shape with striking similarity to the experiment and is only slightly blue-shifted from the experiment by 10 nm (Figure 4d). The distance from opposite points on the face of a hexagon, between In atoms on the face of a hexagon, and between hexagons is calculated to be 5.093, 3.788, and 2.615 Å respectively. The close match between theoretical results and experimental data allows assignment of Raman peaks at 114 $cm^{-1}$ and 220 $cm^{-1}$ to $InS_2$ scissoring in the cage and $InS_2$ wagging in the cage, respectively. This DFT-based UV−visible absorbance simulation allows assignment of the shoulder at 280 nm to excitations with the most contribution from HOMO to LUMO transition and the peak at 264 nm to excitations with primary contribution from HOMO−1 to LUMO (Figure 4e). More detailed discussion and the electronic density of each molecular orbital can be seen in Supporting Information Figure S6.

A possible mechanism for $In_6S_6(CH_3)_6$ MSC formation was informed by first-principles calculation. Both the free energies of possible intermediate species and the kinetic energy barrier, which was deduced from transition states in each reaction, were considered. Consistent with our chemical intuition for proton-mediated ligand exchange, the calculations predict that exposure of TMIn in PMMA to $H_2S$ will form $In(SH)(CH_3)_2$ and methane, with $\Delta G_{433.15\ K} = -1.51$ eV and a kinetic barrier of 0.34 eV (Scheme 2a). After forming $In(SH)(CH_3)_2$, two subsequent competing reactions were considered; growth to an $In_2S(CH_3)_4$ dimer through condensation of two $In(SH)(CH_3)_2$ or further reaction with $H_2S$ to form $In(SH)_2CH_3$ and another $CH_4$ (Scheme 2b and Supporting Information Figure S7). In the latter, the formation of $In_2S(CH_3)_4$ requires multiple steps and also requires overcoming a kinetic barrier (1.38 eV) that is higher than that of $In(SH)_2CH_3$ formation (0.66 eV). Therefore, we continued the mechanistic pathway through $InCH_3(SH)_2$. Further subsequent reactions may include loss of the final methyl group through reaction with a third $H_2S$ or condensation of two $In(SH)_2CH_3$ to form an $In_2S_2(CH_3)_2$ dimer (Scheme 2c). While we calculate $In(SH)_3$ to be more stable than $In_2S_2(CH_3)_2$ by 0.9 eV, the kinetic energy barrier to form $In(SH)_3$ is 0.78 eV, in contrast to the barrierless formation of $In_2S_2(CH_3)_2$, in the absence of a transition state. Dimer formation at this stage is also consistent with vibrational spectroscopy evidence of methyl groups in the resulting clusters. Two possible pathways were considered after formation of the $In_2S_2(CH_3)_2$ dimer, all which are a continuation of a reaction sequence initiated by TMIn exposure to $H_2S$ (i.e., in a single SIS cycle). First, we considered the formation of a hexagonal trimer, $In_3S_3(CH_3)_3$, but that would require two In−S bonds to be broken (with a considerable kinetic barrier) in order to form a hexagonal trimer directly from the $In_2S_2(CH_3)_2$ framework. In contrast, a ribbon-shaped $In_3S_3(CH_3)_3$ trimer may easily form without breaking the In−S bonds (Scheme 2d). The ribbon configuration of $In_3S_3(CH_3)_3$ is also 0.05 eV lower in energy than that of the hexagonal structure. The simulated UV absorbance of the ribbon-shaped $In_3S_3(CH_3)_3$ trimer is also similar to that after a single SIS cycle (see Supporting Information Figure S8). As such, we hypothesize that the ribbon-shaped $In_3S_3(CH_3)_3$ is favored to be formed at low fragment concentrations. As the concentration of ribbon-shaped $In_3S_3(CH_3)_3$ increases, we calculated favorable condensation to form $In_6S_6(CH_3)_6$ (Scheme 2e). Further condensation to an even larger cluster (i.e., $In_{12}S_{12}(CH_3)_{12}$) from two $In_6S_6(CH_3)_6$ is theoretically possible but would require 5 coordinate In to connect a 4-stack of hexagonal trimers. To our best knowledge, 5 coordinate In is far less


https://doi.org/10.1021/acsnano.4c10943
ACS Nano 2024, 18, 31372−31380

**Scheme 2. Calculated Reaction Thermodynamics for $In_6S_6(CH_3)_6$ Formation at the MN15/CEP-121G Level of Theory[a]**

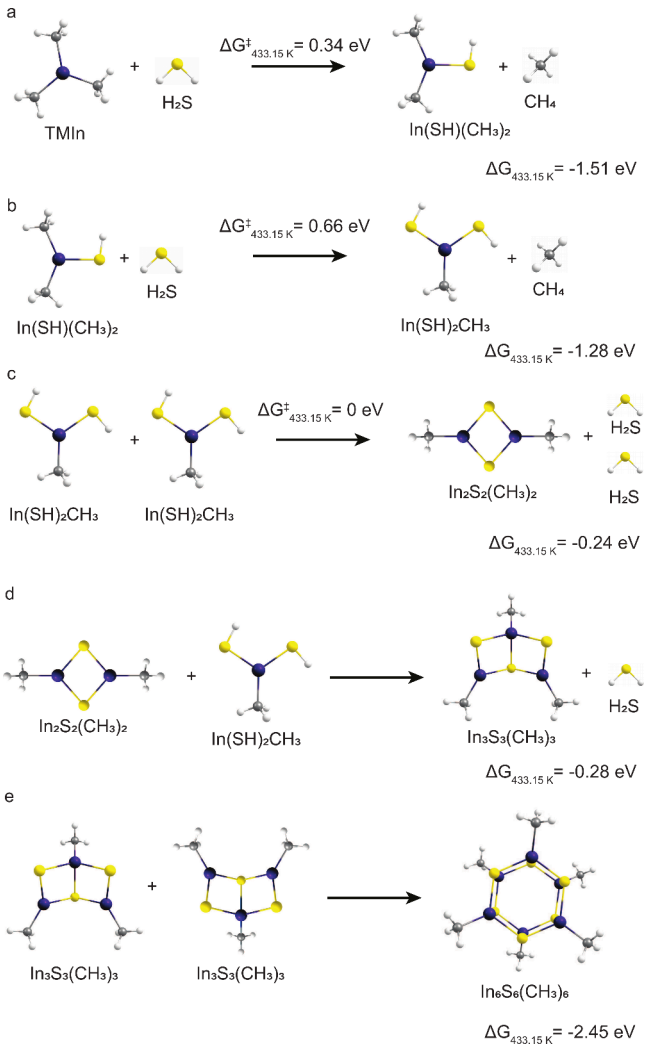


[a]The reaction temperature was set to 160 °C. $\Delta G$ and $\Delta G^{\ddagger}$ represent free energy and kinetic barrier of each reaction respectively.

common than 4 coordinate In. Therefore, we hypothesize the majority structure to be an $In_6S_6(CH_3)_6$ MSC.[62,63]

Evidence for $In_6S_6(CH_3)_6$ MSCs was observed over a range of SIS process conditions; however, it was possible to move outside the apparent MSC process window through significant reduction of the SIS reaction temperature. SIS growth temperatures from 80 to 160 °C were explored (see Figure 5) with the bound on the SIS process temperature that corresponds to the stiction temperature of the Kalrez O-ring that seals the ALD/SIS reactor and the PMMA melting temperature, respectively. At lower temperatures, the overall optical absorbance intensity increased, consistent with previous reports of slower adduct dissociation at lower temperatures that lead to more nucleation events for the same purge time after the metal precursor dose.[18] The overall spectral line shape at lower reaction temperatures is significantly broadened due to the relative intensity increase between 270 and 285 nm as well as 220−250 nm (Supporting Information Figure S9). The relative intensity of wavelengths less than 225 nm was increased markedly below 140 °C. The primary peak around

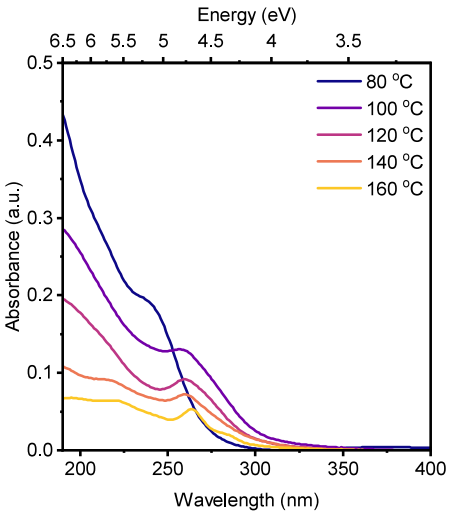


**Figure 5. Absorbance spectra with variation of reaction temperatures. The number of SIS cycles and $N_2$ purging time were fixed to 9 and 480 s, respectively.**

260 nm is gradually blue-shifted and broadened until 100 °C. At the lowest SIS temperature that we attempted (80 °C) the primary low energy feature (264 nm peak) was shifted to 238 nm and the absorbance edge shifted to from >300 to 280 nm. This suggests that the resulting inorganic deposit at 80 °C is distinct from the MSC formed at 160 °C. This hypothesis is further supported by a significantly reduced stability upon air exposure (Supporting Information Figure S10). When the deposit that was synthesized at 80 °C was exposed to air, the intensity of the 240 nm peak was reduced over hours to produce a new shoulder near 255 nm. In contrast, the $In_6S_6(CH_3)_6$ MSC synthesized at 160 °C showed good air stability for more than 24 h.

## CONCLUSIONS

The sequential infiltration of a volatile organometallic In precursor and $H_2S$ results in an indium chalcogenide deposit in multiple polymer thin films. Experimental and computational structure studies are consistent with a methyl-terminated $In_6S_6(CH_3)_6$ MSC. In contrast to conventional island growth via ALD, multiple precursor exposure cycles produce a deposit that is consistent with an increasing concentration of identical MSCs in the polymer thin film. In contrast to the challenging and time-consuming purification processes required for the solution phase syntheses of some MSCs, SIS allows volatile excess precursors and byproducts to be rapidly removed through $N_2$ purging under a low vacuum. Formation of the same $In_6S_6(CH_3)_6$ cluster is favored in PAA and PVDF, however, a significantly lower reaction temperature is sufficient to alter the reaction pathways to produce a less well-defined deposit that is unstable to air exposure. This route to the direct deposition of molecularly precise MSCs in thin film format may inspire use in device applications, as well as the use of other volatile organometallic ALD precursors with moderate reactivity in the synthesis of molecularly precise arrangements of countable atom number clusters.

## EXPERIMENT

**Materials.** Trimethylindium (TMIn, 98+ %) was purchased from Strem, hydrogen sulfide ($H_2S$), polymethylmetacrylate (PMMA), (15000 average MW), poly(acrylic acid) (PAA),


https://doi.org/10.1021/acsnano.4c10943
ACS Nano 2024, 18, 31372−31380

poly(vinylidene fluoride) (PVDF), N,N-dimethylformamide (DMF), and toluene 99.8% were purchased from Sigma-Aldrich (99.99%).

**Polymer Thin Film Preparation.** Silicon and fused quartz substrates were cleaned by submersion into acetone followed by sonication for 30 min. Next the substrate was rinsed with isopropyl alcohol and dried with an air gun. The dried substrates were treated in a UV ozone cleaner for 10 min to remove any residual organics. PMMA was dissolved in toluene with vigorous stirring to produce an 8 wt % solution and filtered with 0.45 $\mu$m pore size syringe filter. The filtered PMMA solution was spin-coated at 3000 rpm to form a 320 nm thickness. PAA was dissolved in water (5 wt %) and filtered with a 0.45 $\mu$m pore size syringe filter. The filtered PAA solution was spin-coated on freshly prepared substrates at 3000 rpm to form a 262 nm thickness. 7 wt % PVDF solutions were prepared by dissolving in DMF solvent. The PVDF solution was also filtered with a 0.45 $\mu$m pore size syringe filter and spin-coated at 5000 rpm to form a 153 nm thickness. The prepared polymer layers were dried in the Veeco/Cambridge Savannah ALD growth chamber at 160 °C under 20 sccm $N_2$ flow for 30 min to remove any remaining trace solvent and moisture.

**SIS.** Sequential infiltration synthesis experiments were conducted in a Veeco/Cambridge Savannah 200 ALD instrument at 160 °C. The TMIn precursor was heated at 50 °C to increase the vapor pressure. Safety note: TMIn is a volatile pyrophoric solid that requires air-free handling and must not be excessively heated. All processes utilized a constant $N_2$ flow of 20 sccm. PMMA films were held in the chamber under a $N_2$ flow and rough vacuum for 5 min before beginning SIS. One complete SIS cycle consisted of a dose, exposure, and purge, for both TMIn and $H_2S$. Just prior to the dose step, the growth chamber is isolated from the vacuum, and the desired precursor is allowed to fill the chamber under its own vapor pressure for a specific dose time. Only additional $N_2$ is allowed to flow into the sealed growth chamber during the exposure step. Finally, the growth chamber is opened back to a rough vacuum while maintaining a $N_2$ gas flow. In this work, unless otherwise noted, each complete SIS cycle consists of a 3 s dose of TMIn (2 Torr), 63 s of total exposure to TMIn, and 480 s of $N_2$ purge followed by a 0.2 s dose of $H_2S$ (30 Torr), 62 s total exposure to $H_2S$, and 480 s of $N_2$ purge.

## ASSOCIATED CONTENT

### Supporting Information

The Supporting Information is available free of charge at https://pubs.acs.org/doi/10.1021/acsnano.4c10943.

> The details of the following methodologies also used in this work - specifically: AEM, RAMAN, UV, NIR, FTIR, XPS, Ellipsometery and Computations are presented in the Supporting Information materials of this paper. (PDF)

## AUTHOR INFORMATION


### Corresponding Author

**Alex B. F. Martinson** − *Material Science Division, Argonne National Laboratory, Lemont, Illinois 60439, United States;* orcid.org/0000-0003-3916-1672; Email: martinson@anl.gov

### Authors

**Kihoon Kim** − *Material Science Division, Argonne National Laboratory, Lemont, Illinois 60439, United States;* orcid.org/0000-0003-1034-9233

**Shana Havenridge** − *Chemical Science and Engineering Division, Argonne National Laboratory, Lemont, Illinois 60439, United States;* orcid.org/0000-0001-8481-0585

**Nestor J. Zaluzec** − *University of Chicago, Pritzer School of Molecular Engineering, Chicago, Illinois 60637, United States; Photon Sciences Directorate, Argonne National Laboratory, Lemont, Illinois 60439, United States*

**Donghyeon Kang** − *Applied Materials Division, Argonne National Laboratory, Lemont, Illinois 60439, United States;* orcid.org/0000-0003-3960-0823

**Nuwanthaka P. Jayaweera** − *Material Science Division, Argonne National Laboratory, Lemont, Illinois 60439, United States;* orcid.org/0000-0003-4707-9118

**Jeffrey W. Elam** − *Applied Materials Division, Argonne National Laboratory, Lemont, Illinois 60439, United States;* orcid.org/0000-0002-5861-2996

**Karen L. Mulfort** − *Chemical Science and Engineering Division, Argonne National Laboratory, Lemont, Illinois 60439, United States;* orcid.org/0000-0002-3132-1179

**Cong Liu** − *Chemical Science and Engineering Division, Argonne National Laboratory, Lemont, Illinois 60439, United States;* orcid.org/0000-0002-2145-5034

Complete contact information is available at: https://pubs.acs.org/10.1021/acsnano.4c10943


### Author Contributions

K.K. and A.B.F.M. conceived the idea and designed the experiments. Experiments were performed by K.K. and N.J. N.J.Z. and K.K. performed STEM imaging and analysis. XPS characterization was performed by D.K., J.W.E., and K.K. S.H. and C.L performed simulations. All authors discussed the approach and the results and were involved in the manuscript writing. A.B.F.M. and K.L.M. supervised the project.

### Notes

The authors declare no competing financial interest.

## ACKNOWLEDGMENTS

This work was supported by the U.S. Department of Energy, Office of Science, Office of Basic Energy Sciences, Division of Chemical Sciences, Geosciences, and Biosciences at Argonne National Laboratory (ANL) under Contract No. DE-AC02-06CH11357. The Analytical Picoprobe Electron Microscope (ThermoFisher Scientific Spectra Ultra X) was developed as part of a CRADA #01300710 between ANL and ThermoFisher Scientific Instruments. The PicoProbe/STEM imaging was also supported by the National Science Foundation Major Research Instrumentation (MRI) Program (NSF DMR-2117896) at the University of Chicago. S.H. and C. L. acknowledge the computational support from Bebop cluster of Laboratory Computational Resource Center (LCRC) at Argonne National Laboratory.

## REFERENCES

(1) Bootharaju, M. S.; Baek, W.; Deng, G.; Singh, K.; Voznyy, O.; Zheng, N.; Hyeon, T. Structure of a subnanometer-sized semiconductor $Cd_{14}Se_{13}$ cluster. *Chem.* **2022**, *8*, 2978−2989.

(2) Johns, R. W.; Bechtel, H. A.; Runnerstrom, E. L.; Agrawal, A.; Lounis, S. D.; Milliron, D. J. Direct observation of narrow mid-

infrared plasmon linewidths of single metal oxide nanocrystals. *Nat. Commun.* **2016**, *7*, 11583.
(3) Friedfeld, M. R.; Stein, J. L.; Ritchhart, A.; Cossairt, B. M. Conversion reactions of atomically precise semiconductor clusters. *Acc. Chem. Res.* **2018**, *51*, 2803−2810.
(4) Kasuya, A.; Sivamohan, R.; Barnakov, Y. A.; Dmitruk, I. M.; Nirasawa, T.; Romanyuk, V. R.; Kumar, V.; Mamykin, S. V.; Tohji, K.; Jeyadevan, B.; et al. Ultra-stable nanoparticles of CdSe revealed from mass spectrometry. *Nat. Mater.* **2004**, *3*, 99−102.
(5) Lee, J.; Yang, J.; Kwon, S. G.; Hyeon, T. Nonclassical nucleation and growth of inorganic nanoparticles. *Nat. Rev. Mater.* **2016**, *1*, 1−16.
(6) Williamson, C. B.; Nevers, D. R.; Nelson, A.; Hadar, I.; Banin, U.; Hanrath, T.; Robinson, R. D. Chemically reversible isomerization of inorganic clusters. *Science* **2019**, *363*, 731−735.
(7) Gary, D. C.; Flowers, S. E.; Kaminsky, W.; Petrone, A.; Li, X.; Cossairt, B. M. Single-crystal and electronic structure of a 1.3 nm indium phosphide nanocluster. *J. Am. Chem. Soc.* **2016**, *138*, 1510−1513.
(8) Palencia, C.; Yu, K.; Boldt, K. The future of colloidal semiconductor magic-size clusters. *ACS Nano* **2020**, *14*, 1227−1235.
(9) Fernando, A.; Weerawardene, K. D. M.; Karimova, N. V.; Aikens, C. M. Quantum mechanical studies of large metal, metal oxide, and metal chalcogenide nanoparticles and clusters. *Chem. Rev.* **2015**, *115*, 6112−6216.
(10) Busatto, S.; de Mello Donega, C. Magic-size semiconductor nanostructures: where does the magic come from? *ACS Mater. Au* **2022**, *2*, 237−249.
(11) Mule, A. S.; et al. Unraveling the growth mechanism of magic-sized semiconductor nanocrystals. *J. Am. Chem. Soc.* **2021**, *143*, 2037−2048.
(12) Gary, D. C.; Terban, M. W.; Billinge, S. J.; Cossairt, B. M. Two-step nucleation and growth of InP quantum dots via magic-sized cluster intermediates. *Chem. Mater.* **2015**, *27*, 1432−1441.
(13) Jena, P.; Sun, Q. Super atomic clusters: design rules and potential for building blocks of materials. *Chem. Rev.* **2018**, *118*, 5755−5870.
(14) Kudera, S.; et al. Sequential growth of magic-size CdSe nanocrystals. *Adv. Mater.* **2007**, *19*, 548−552.
(15) Jiang, Y.; et al. Synthesis-on-substrate of quantum dot solids. *Nature* **2022**, *612*, 679−684.
(16) Forte, M. A.; Silva, R. M.; Tavares, C. J.; Silva, R. F. e. Is poly (Methyl Methacrylate)(PMMA) a suitable substrate for ALD?: A review. *Polymers* **2021**, *13*, 1346.
(17) He, X.; Waldman, R. Z.; Mandia, D. J.; Jeon, N.; Zaluzec, N. J.; Borkiewicz, O. J.; Ruett, U.; Darling, S. B.; Martinson, A. B.; Tiede, D. M. Resolving the atomic structure of sequential infiltration synthesis derived inorganic clusters. *ACS Nano* **2020**, *14*, 14846−14860.
(18) Weisbord, I.; Shomrat, N.; Azoulay, R.; Kaushansky, A.; Segal-Peretz, T. Understanding and controlling polymer−organometallic precursor interactions in sequential infiltration synthesis. *Chem. Mater.* **2020**, *32*, 4499−4508.
(19) Waldman, R. Z.; Jeon, N.; Mandia, D. J.; Heinonen, O.; Darling, S. B.; Martinson, A. B. Sequential infiltration synthesis of electronic materials: Group 13 oxides via metal alkyl precursors. *Chem. Mater.* **2019**, *31*, 5274−5285.
(20) Waldman, R. Z.; Mandia, D. J.; Yanguas-Gil, A.; Martinson, A. B.; Elam, J. W.; Darling, S. B. The chemical physics of sequential infiltration synthesis—A thermodynamic and kinetic perspective. *J. Chem. Phys.* **2019**, *151*, 190901.
(21) Ye, X.; Kestell, J.; Kisslinger, K.; Liu, M.; Grubbs, R. B.; Boscoboinik, J. A.; Nam, C.-Y. Effects of residual solvent molecules facilitating the infiltration synthesis of ZnO in a nonreactive polymer. *Chem. Mater.* **2017**, *29*, 4535−4545.
(22) Peng, Q.; Tseng, Y.-C.; Long, Y.; Mane, A. U.; DiDona, S.; Darling, S. B.; Elam, J. W. Effect of nanostructured domains in self-assembled block copolymer films on sequential infiltration synthesis. *Langmuir* **2017**, *33*, 13214−13223.
(23) Kim, J. J.; et al. Mechanistic understanding of tungsten oxide in-plane nanostructure growth via sequential infiltration synthesis. *Nanoscale* **2018**, *10*, 3469−3479.
(24) Barick, B. K.; Simon, A.; Weisbord, I.; Shomrat, N.; Segal-Peretz, T. Tin oxide nanostructure fabrication via sequential infiltration synthesis in block copolymer thin films. *J. Colloid Interface Sci.* **2019**, *557*, 537−545.
(25) Yi, D. H.; Nam, C.-Y.; Doerk, G.; Black, C. T.; Grubbs, R. B. Infiltration synthesis of diverse metal oxide nanostructures from epoxidized diene−styrene block copolymer templates. *ACS Appl. Polym. Mater.* **2019**, *1*, 672−683.
(26) Dusoe, K. J.; Ye, X.; Kisslinger, K.; Stein, A.; Lee, S.-W.; Nam, C.-Y. Ultrahigh elastic strain energy storage in metal-oxide-infiltrated patterned hybrid polymer nanocomposites. *Nano Lett.* **2017**, *17*, 7416−7423.
(27) Berman, D.; Guha, S.; Lee, B.; Elam, J. W.; Darling, S. B.; Shevchenko, E. V. Sequential infiltration synthesis for the design of low refractive index surface coatings with controllable thickness. *ACS Nano* **2017**, *11*, 2521−2530.
(28) Tseng, Y.-C.; Peng, Q.; Ocola, L. E.; Elam, J. W.; Darling, S. B. Enhanced block copolymer lithography using sequential infiltration synthesis. *J. Phys. Chem. C* **2011**, *115*, 17725−17729.
(29) She, Y.; Goodman, E. D.; Lee, J.; Diroll, B. T.; Cargnello, M.; Shevchenko, E. V.; Berman, D. Block-co-polymer-assisted synthesis of all inorganic highly porous heterostructures with highly accessible thermally stable functional centers. *ACS Appl. Mater. Interfaces* **2019**, *11*, 30154−30162.
(30) Allen, J. E.; Ray, B.; Khan, M. R.; Yager, K. G.; Alam, M. A.; Black, C. T. Self-assembly of single dielectric nanoparticle layers and integration in polymer-based solar cells. *Appl. Phys. Lett.* **2012**, *101*, 063105.
(31) McGuinness, E. K.; Zhang, F.; Ma, Y.; Lively, R. P.; Losego, M. D. Vapor phase infiltration of metal oxides into nanoporous polymers for organic solvent separation membranes. *Chem. Mater.* **2019**, *31*, 5509−5518.
(32) Zhou, C.; Segal-Peretz, T.; Oruc, M. E.; Suh, H. S.; Wu, G.; Nealey, P. F. Fabrication of nanoporous alumina ultrafiltration membrane with tunable pore size using block copolymer templates. *Adv. Funct. Mater.* **2017**, *27*, 1701756.
(33) Segal-Peretz, T.; et al. Characterizing the three-dimensional structure of block copolymers via sequential infiltration synthesis and scanning transmission electron tomography. *ACS Nano* **2015**, *9*, 5333−5347.
(34) Kunene, T.; Martinson, A. B. Understanding the unique optical and vibrational signatures of sequential infiltration synthesis derived indium oxyhydroxide clusters for $CO_2$ absorption. *J. Vac. Sci. Technol. A* **2023**, *41*, 042402.
(35) Park, Y.-S.; Roh, J.; Diroll, B. T.; Schaller, R. D.; Klimov, V. I. Colloidal quantum dot lasers. *Nat. Rev. Mater.* **2021**, *6*, 382−401.
(36) Giri, A.; Park, G.; Jeong, U. Layer-structured anisotropic metal chalcogenides: recent advances in synthesis, modulation, and applications. *Chem. Rev.* **2023**, *123*, 3329−3442.
(37) Corrigan, J. F.; Fuhr, O.; Fenske, D. Metal chalcogenide clusters on the border between molecules and materials. *Adv. Mater.* **2009**, *21*, 1867−1871.
(38) Chi, L.-P.; Niu, Z.-Z.; Zhang, X.-L.; Yang, P.-P.; Liao, J.; Gao, F.-Y.; Wu, Z.-Z.; Tang, K.-B.; Gao, M.-R. Stabilizing indium sulfide for $CO_2$ electroreduction to formate at high rate by zinc incorporation. *Nat. Commun.* **2021**, *12*, 5835.
(39) Huang, W.; Gan, L.; Yang, H.; Zhou, N.; Wang, R.; Wu, W.; Li, H.; Ma, Y.; Zeng, H.; Zhai, T. Controlled synthesis of ultrathin 2D $\beta$-$In_2S_3$ with broadband photoresponse by chemical vapor deposition. *Adv. Funct. Mater.* **2017**, *27*, 1702448.
(40) Zhang, H.; et al. Dissociation-assembly-carbonization: A strategy for constructing indium sulfide photocatalysts with increased reactive sites and spatial charge separation. *ACS Catal.* **2023**, *13*, 14657−14669.


https://doi.org/10.1021/acsnano.4c10943
*ACS Nano* 2024, 18, 31372−31380

(41) Gao, M.-R.; Xu, Y.-F.; Jiang, J.; Yu, S.-H. Nanostructured metal chalcogenides: synthesis, modification, and applications in energy conversion and storage devices. *Chem. Soc. Rev.* **2013**, *42*, 2986−3017.
(42) Lee, B. R.; Jang, H. W. $\beta$-$In_2S_3$ as water splitting photoanodes: promise and challenges. *Electron. Mater. Lett.* **2021**, *17*, 119−135.
(43) Lee, Y. K.; Yoo, C.; Kim, W.; Jeon, J. W.; Hwang, C. S. Atomic layer deposition of chalcogenides for next-generation phase change memory. *J. Mater. Chem. C* **2021**, *9*, 3708−3725.
(44) McCarthy, R. F.; Weimer, M. S.; Emery, J. D.; Hock, A. S.; Martinson, A. B. Oxygen-free atomic layer deposition of indium sulfide. *ACS Appl. Mater. Interfaces* **2014**, *6*, 12137−12145.
(45) Lei, Z.-X.; Zhu, Q.-Y.; Zhang, M.-H.; Jiang, J.-B.; Zhang, Y.-P.; Dai, J. Indium chalcogenido clusters coordinated by 1,10-Phenanthroline,$[InQ (phen) Cl]_4$ (Q= Se, S), a simplified model of inorganic-organic hybrid material with cluster-to-ligand charge transfer. *Inorg. Chem.* **2010**, *49*, 353−355.
(46) Wu, T.; Zuo, F.; Wang, L.; Bu, X.; Zheng, S.-T.; Ma, R.; Feng, P. A large indium sulfide supertetrahedral cluster built from integration of ZnS-like tetrahedral shell with NaCl-like octahedral core. *J. Am. Chem. Soc.* **2011**, *133*, 15886−15889.
(47) Kim, K.; Yu, J.; Noh, J.; Reimnitz, L. C.; Chang, M.; Gamelin, D. R.; Korgel, B. A.; Hwang, G. S.; Milliron, D. J. Synthetic control of intrinsic defect formation in metal oxide nanocrystals using dissociated spectator metal salts. *J. Am. Chem. Soc.* **2022**, *144*, 22941−22949.
(48) Ramirez, E.; Erades, L.; Philippot, K.; Lecante, P.; Chaudret, B. Shape control of platinum nanoparticles. *Adv. Funct. Mater.* **2007**, *17*, 2219−2228.
(49) Knecht, T. A.; Hutchison, J. E. Precursor and surface reactivities influence the early growth of indium oxide nanocrystals in a reagent-driven, continuous addition synthesis. *Chem. Mater.* **2023**, *35*, 3151−3161.
(50) Lai, W.-H.; Wang, Y.-X.; Wang, Y.; Wu, M.; Wang, J.-Z.; Liu, H.-K.; Chou, S.-L.; Chen, J.; Dou, S.-X. Morphology tuning of inorganic nanomaterials grown by precipitation through control of electrolytic dissociation and supersaturation. *Nat. Chem.* **2019**, *11*, 695−701.
(51) Lin, H.-x.; Lei, Z.-c.; Jiang, Z.-y.; Hou, C.-p.; Liu, D.-y.; Xu, M.-m.; Tian, Z.-q.; Xie, Z.-x. Supersaturation-dependent surface structure evolution: from ionic, molecular to metallic micro/nanocrystals. *J. Am. Chem. Soc.* **2013**, *135*, 9311−9314.
(52) Cho, S. H.; et al. Syntheses of colloidal F: $In_2O_3$ cubes: Fluorine-induced faceting and infrared plasmonic response. *Chem. Mater.* **2019**, *31*, 2661−2676.
(53) Narayanaswamy, A.; Xu, H.; Pradhan, N.; Kim, M.; Peng, X. Formation of nearly monodisperse $In_2O_3$ nanodots and oriented-attached nanoflowers: hydrolysis and alcoholysis vs pyrolysis. *J. Am. Chem. Soc.* **2006**, *128*, 10310−10319.
(54) Kurbakova, A.; Bukalov, S.; Leites, L.; Golubinskaya, L.; Bregadze, V. Vibrational spectra and structure of trimethylindium and trimethylthallium. *J. Organomet. Chem.* **1997**, *536*, 519−529.
(55) Hall, J.; Woodward, L.; Ebsworth, E. Raman and infra-red spectra of gallium trimethyl and indium trimethyl. *Spectrochim. Acta* **1964**, *20*, 1249−1256.
(56) Dasgupta, N. P.; Meng, X.; Elam, J. W.; Martinson, A. B. Atomic layer deposition of metal sulfide materials. *Acc. Chem. Res.* **2015**, *48*, 341−348.
(57) Lee, H. J.; Hwang, J. H.; Park, J.-Y.; Lee, S. W. Alternative surface reaction route in the atomic layer deposition of titanium nitride thin films for electrode applications. *ACS Appl. Electron. Mater.* **2021**, *3*, 999−1005.
(58) Jewell, C. F.; Subramanian, A.; Lee, W.-I.; Nam, C.-Y.; Finke, R. G. Overcoming residual carbon-induced recombination in water-oxidation catalysis: combining a superior catalyst with low-carbon-content atomic layer deposition of $SnO_2$ for improved catalysis. *Sustain. Energy Fuels* **2023**, *7*, 4567−4579.
(59) Raghunath, P.; Lin, M.-C. Computational study on the mechanisms and energetics of trimethylindium reactions with $H_2O$ and $H_2S$. *J. Phys. Chem. A* **2007**, *111*, 6481−6488.
(60) Xu, H.; Wang, Y.; Dong, X.; Zheng, N.; Ma, H.; Zhang, X. Fabrication of $In_2O_3/In_2S_3$ microsphere heterostructures for efficient and stable photocatalytic nitrogen fixation. *Appl. Catal. B: Environ.* **2019**, *257*, 117932.
(61) Yan, D.; Wan, Z.; Wang, K.; Wang, X. $In_2O_3/In_2S_3$ heterostructures derived from In-MOFs with enhanced visible light photocatalytic performance for $CO_2$ reduction. *ChemistrySelect* **2021**, *6*, 2508−2515.
(62) Leman, J. T.; Roman, H. A.; Barron, A. R. Five-and six-coordinate organometallic compounds of indium. *Organometallics* **1993**, *12*, 2986−2990.
(63) Kuo, P.-C.; Huang, J.-H.; Hung, C.-H.; Lee, G.-H.; Peng, S.-M. Synthesis and characterization of five-coordinate gallium and indium complexes stabilized by tridentate, substituted pyrrole ligands. *Eur. J. Inorg. Chem.* **2003**, *2003*, 1440−1444.




https://doi.org/10.1021/acsnano.4c10943
*ACS Nano* 2024, 18, 31372−31380